Control of the Nanopositioning Devices

Srinivasa Salapaka
svasu@mit.edu, Laboratory for Information and Decision Systems, MIT, MA 02139
Abu Sebastian
abuseb@iastate.edu, Department of Electrical and Computer Engineering, Iowa State University, Ames, IA 50011

Abstract—We present a paradigm which prescribes a procedure for a systematic design, analysis and development of nanopositioning devices. In this effort, we have used many tools from modern control theory to model devices, to quantify device resolution, bandwidth, range, and robustness, and to tackle undesirable nonlinear effects such as hysteresis and creep. The implementation of this procedure for the *simultaneous* achievement of robustness, high precision, and high bandwidth objectives is presented. Emphasis is placed on the robustness aspects that make the nanopositioner operable in diverse operating conditions thus alleviating the need for tuning that is present in existing designs. The merits of the paradigm are demonstrated through experimental results.

I. INTRODUCTION

One of the pivotal requirements of nanotechnology is nanopositioning. The interrogation and manipulation at atomic scales demands positioning systems with atomic scale resolutions. For example nanopositioning systems are necessary in scanning probe microscopy to provide subnanometer-resolution motions in order to probe molecular and atomic features on a sample, in test equipments' for semiconductors such as mask and wafer inspection systems [1], in grading and testing disk drive read-write heads [2], in characterizing magnetic media and recording methods, in optical alignment systems [3], [4], in molecular biology [5], [6], and in synchotrons for X-ray microscopy.

Typically, the nanopositioning devices are actuated by piezoelectric materials. The crystal lattices of these materials deform on application of an electric field. These deformations are used for accurate positioning. The advantages of these actuators are several: they provide repeatable sub-nanometer motion, do not have backlash, do not suffer from wear and tear, require very little maintenance, have fast response times, can generate large forces, are operable in a wide range of temperatures, and are not affected by magnetic fields. However, their use is hindered by nonlinear effects like hysteresis and creep. Hysteretic effects, in which the piezo motion does not vary linearly with the applied voltage are prominent especially in large traversals and can be as high as 10-15% of the path covered. Creep, in which the piezo drifts independent of the applied voltage, becomes noticeable when positioning is required over long time periods.

There have been many efforts to counter the nonlinear effects which include design changes in the open-loop implementation such as: using 'harder' piezoceramics which have smaller nonlinear effects at the cost of travel range (see Ref. [7]); replacing voltage control by charge control (see Ref. [8]) which achieves lower hysteresis but leads to more creep, lesser travel and lower positioning bandwidth; post processing data obtained from actuations designed for pre-specified trajectories (see Ref. [9]), which are not useful for applications that need real time compensations; and compensating for the adverse nonlinear effects by a careful modelling of the nonlinearities which achieves good results but is sensitive to the precision of the model used (see Ref. [10]). In comparison to the open loop architecture there are fewer feedback design schemes for nanopositioning. In Ref. [11], the design of a feedback controller using an optical sensor attachment to enhance the performance of an Atomic Force Microscope scanner is described. Similar efforts to improve the scanning speeds of the AFM are made in Ref. [12]. Ref. [13] describes the $\mathcal{H}_\infty$ controller design for a one dimensional nanopositioning system where high closed loop bandwidths are achieved.

The feedback laws, when employed in nanopositioning industry, are usually Proportional Integral (PI) or Proportional double integral (PII) control laws. These laws provide high gains at low frequencies and greatly diminish the hysteretic and creep effects. However, they achieve very low bandwidths and have poor robustness properties. This low bandwidth can be explained from the following simplified

analysis. The transfer functions representing the nanopositioning systems usually have very low damping values for the slowest modes. So, if we approximate the system by considering only its slow modes $x \pm iy$, the PI control law results in a third order closed loop system where the characteristic polynomial is given by $s^3 + 2\delta\omega_n s^2 + (k_p + w_n^2)s + k_i$, where $\omega_n \triangleq \sqrt{(x^2 + y^2)}$ and $\delta \triangleq x/\omega_n$. For this system the bandwidth is in the order of $\delta\omega_n$. For the devices that we studied ω_n was approximately $400\,Hz$ and the damping δ was around 0.008 which gives an estimate of $3.2\,Hz$ on the bandwidth.

In this paper, we present the importance of modern control theoretic tools in addressing these demands and challenges on the nanopositioning systems. The compensation of the hysteretic and creep effects form only a small portion of the demands on the design. The main design challenges come from the demands on the bandwidth, precision and robustness. We show how many of the popular approaches in the nanopositioning industry are inadequate in obtaining simultaneously these objectives while the modern control approach, in contrast, provides an apt paradigm to incorporate these objectives, obtain models of these devices, to quantify device in terms of resolution, bandwidth, range and sensitivity, and tackle hysteresis and creep. In particular, we present the $\mathcal{H}_\infty$ control designs (nominal, robust and Glover-McFarlane) and contrast it with the more prevalent proportional integral (PI) and proportional double integral (PII) designs. We demonstrate this approach through a design of a nanopositioning system Our contributions in this paper are two fold: (1) identification of demands and challenges in nanopositioning systems and their translation to the control paradigm, and (2) application of this paradigm in designing, building and characterizing nanopositioning devices with a special emphasis on the bandwidth, resolution and robustness. The justification and the study of the impact of implementing $\mathcal{H}_\infty$ and Glover McFarlane control designs in view of *simultaneously* achieving performance and robustness form the main emphasis of this paper. We demonstrate this through the control designs of devices that we have developed by reviewing some of the designs presented in [13] and [14] and present some new control designs.

II. NANOPOSITIONING DEVICES

A. One dimensional nanopositioning device

The nanopositioning system studied in this paper is described in Figure 1 (developed in *Asylum Research*, Santa Barbara, California). The main idea is based on the elastic deformation of the flexure stage which is used for nanopositioning. This motion is obtained by the serpentine spring design (see Figure 1) where design grooves (about $150\mu m$ wide) are cut in the base plate, making it possible for the central block containing the sample to move relative to the frame.
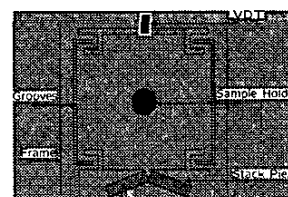

Fig. 1.   A schematic of the nanopositioning device.

The forces to induce elastic deformations are generated by stack-piezos. As shown in Figure 1, these piezo stacks are at an angle $\beta \approx$

7.5 degrees which gives a mechanical gain of $1/\sin(\beta)$. The motion of the flexure stage is measured by the LVDT (Linear Variable Differential Transformer) and the associated demodulation circuit.

The flexure based design has no sliding parts which rules out effects such as backlash. As a result motions with atomic scale resolutions can be obtained. Besides being cheaper, the piezostacks have longer travel ranges compared to their cylindrical counterparts used in commercial AFMs. These actuators lead to a travel range of approximately $75\mu m$. The modified LVDT sensors used in this design have resolution in the order of 2 Å over a 1 kHz bandwidth which gives a vast advantage over more common optical sensors. However, open-loop operation of piezostacks suffers from relatively large effects of hysteresis and creep. This places an added importance to the control system. In this device, the control laws are implemented on a *Texas Instruments C44* digital signal processor.
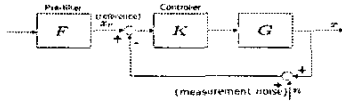

Fig. 2.   A schematic block diagram of the closed loop system.

Figure 2 is a schematic block diagram of the closed loop system. Here x_r represents the reference or the command signal; e denotes the error signal, the difference between the reference and the output signals; and K stands for the controller transfer function. Also, we represent the sensitivity function, i.e., the transfer function from r to e by S; and the complimentary sensitivity function i.e., the transfer function from r to y by T. The tradeoff between achieving high tracking bandwidth and maintaining high resolution translates to designing K such that S is low in the frequencies of reference signals while at the same time rolling off T to mitigate the effects of sensor noise on resolution.

1) Identification of the system: The transfer function G to describe the device was obtained by obtaining its frequency response about an operating point. The nominal operating point is chosen to be the *null position*, i.e. where the LVDT outputs read zero. This was done using a HP signal analyzer which gave a sine sweep of 50 mV signals with frequencies spanning over a bandwidth of 2 kHz. The frequency response of the device at this operating point is shown by the Bode plot (dashed lines) in Figure 3. Accordingly, a fourth order non minimum phase transfer function:

$$G(s) = \frac{9.7 \times 10^4(s - (7.2 \pm 7.4i) \times 10^3)}{(s + (1.9 \pm 4.5i) \times 10^3)(s + (1.2 \pm 15.2i) \times 10^2)}$$

was fit to this data. Figure 3 shows that there is a good match between this frequency response data and the one simulated from the model, $G(s)$.
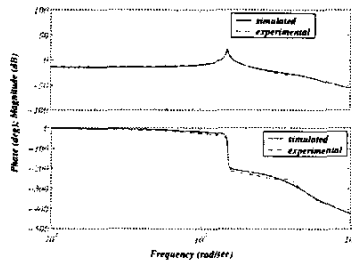

Fig. 3.   A comparison of experimentally obtained and simulated frequency responses of the plant.

2) Control Design: The feedback laws for this device were implemented primarily to achieve high bandwidths ($\approx 150Hz$) and subnanometer resolution. These laws are constrained to provide control signals that were negative and within actuator saturation limits (-10 V to 0 V). Besides these implementation constraints, the presence of RHP zeros imposes fundamental constraints. In
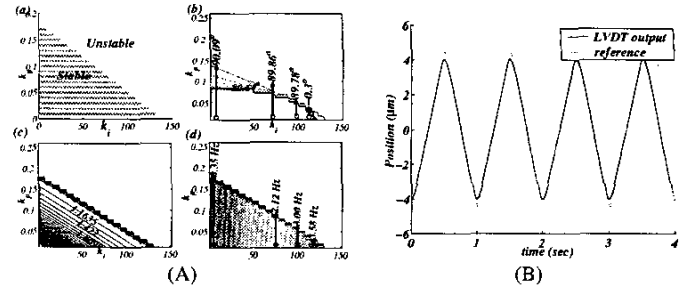

Fig. 4.   (A)(a) The region in k_i-k_p plane that guarantees closed loop stability. The contour plots showing (b)the phase margins (c) the gain margins (d) the bandwidths of the closed loop systems corresponding to different points in the k_i-k_p plane. (B) Tracking of 1 Hz triangular signal with PI controller.

fact these zeros rule out pure gain controllers with gains greater than 0.1674. These zeros also impose a fundamental limit on the achievable bandwidth of the closed loop system. The ideal bandwidth is approximately 415 Hz for the system. This controller is "ideal" in the sense that it may not be realizable and which, for a unit step reference $r(t)$, generates an input $u(t)$ which minimizes the integral square tracking error $\int_0^\infty |y(t) - r(t)|^2 dt$ [15].

PI controller design
Since we know the structure of the controller $(k_p + k_i/s)$, we can determine the regions in the k_p-k_i plane which guarantee closed loop stability. Figure 4(a) shows this plot. It should be noted that the region (in the k_p-k_i plane) that gives high bandwidth (see plot (d)) is the region with low gain margin (see plot (c)), i.e. there is a trade-off between robustness and performance. We chose $k_p = 0.01$ and $k_i = 75$, which guarantee a gain margin of 1.57 and a phase margin of 89° and the corresponding bandwidth of the closed loop transfer function is 2.12 Hz. This controller was implemented and Figure 4(B) shows tracking of a 1 Hz triangular wave. We see that there is an excellent agreement between the reference and the LVDT-output signals for this input.

It should be noted that the bandwidth ($< 3Hz$) attained here is much less than the "ideal" bandwidth (≈ 415 Hz). This low bandwidth agrees well with simplified analysis we presented in Section I. This motivates us to look into more sophisticated designs. We present the design of $\mathcal{H}_\infty$-controller in the next section.

$\mathcal{H}_\infty$ controller design
The main advantage of using this design is that it includes the performance objectives in the problem formulation itself. In order
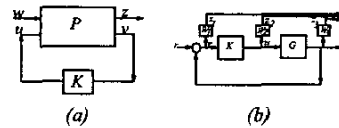

Fig. 5.   (a) The generalized plant framework. (b) The closed loop system with regulated outputs.

to reflect the performance objectives and physical constraints, the regulated outputs were chosen to be the weighted transfer function, $z_1 = W_1 e$, the weighted system output, $z_2 = W_2 y$ and the weighted control input, $z_3 = W_3 u$ (see Figure 5(b)). W_1 was chosen to be a first order transfer function, $W_1(s) = \frac{0.1667s + 2827}{s + 2.827}$. This transfer function is designed so that its inverse (an approximate upper bound on the sensitivity function) has a gain of 0.1% at low frequencies (< 1 Hz) and a gain of $\approx 5\%$ around 200 Hz. We scale the complementary sensitivity function, T, by $W_2 = \frac{s + 235.6}{0.01s + 1414}$ which ensures rolling off of T at high frequencies. The transfer function, KS was scaled by a constant weighting $W_3 = 0.1$, to

restrict the magnitude of the input signals such that they are within the saturation limits. This weighting constant gives control signals that are at most six times the reference signals.
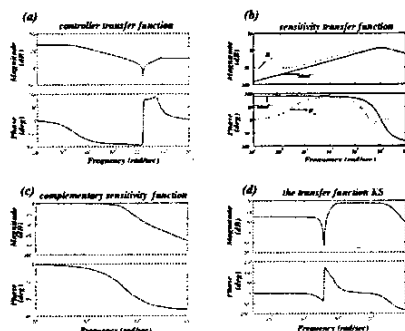

Fig. 6. Closed loop transfer functions: (a)controller (b) sensitivity (c) complementary sensitivity (d)KS

A controller transfer function K such that

$$\| [\ W_1 S \ W_2 T \ W_3 KS \ ] \|_\infty < \gamma$$

where $\gamma = 2.415$ (found iteratively by the control algorithm) was designed using Matlab. The following sixth order controller transfer function, $K(s)$ was obtained with a DC gain of 2.2599×10^3, its poles at $-1.14959 \times 10^7, -1.4137 \times 10^5, -5.6432 \times 10^3, -2.8274$ and $(-1.5676 \pm 5.8438i) \times 10^3$, and its zeroes at $-1.4137 \times 10^5, (-1.8647 \pm 4.4958i) \times 10^3$ and $-1.1713 \times 10^1 \pm 1.5205i \times 10^3$.

The controller, the sensitivity, the complementary sensitivity function and KS transfer functions are shown in Figure 6. The bandwidth of the system (from the sensitivity transfer function) is found to be 138 Hz. It should be noted that this is an enormous improvement over the PI controller. Also, this controller provides a gain margin of 2.57 and a phase margin of $62.3°$ as opposed to the values of 1.57 and 89° in the PI controller.

Figure 7 compares its performance with the PI controller for a 5 Hz triangular wave. It should be noted that the performance of the $\mathcal{H}_\infty$ controller is significantly better than the PI controller. The plot in the right compares the bandwidths obtained by this design. The PI controller achieves a bandwidth of 2.24 Hz while the $\mathcal{H}_\infty$ controller achieves 138.3 Hz - an improvement of over sixty times!

3) Elimination of nonlinear effects: The positioning precision of the piezoactuators is significantly reduced due to nonlinear effects such as hysteresis, drift and creep. However, with the feedback control laws, these nonlinear effects are compensated and thus the closed loop device does not show any hysteresis. The hysteresis plots were obtained by giving input signals (less than 1 Hz triangular pulses) of increasing amplitudes (1 V to 4 V) and recording the corresponding output signals. Then the output vs reference plots were made (see Figure 8(a)). It is observed that the hysteresis effects are dominant at higher amplitudes (longer travels)
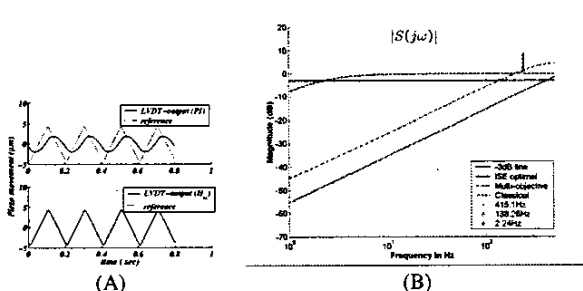

Fig. 7. (A) A comparison of the performance of the closed loop system with (a) PI controller (b) $\mathcal{H}_\infty$ controller. (B) A comparison of bandwidths achieved by PI, $\mathcal{H}_\infty$ and "ideal" controllers.

and become smaller as the travel lengths are reduced. The maximum output hysteresis varies from $0.74\mu m$ to $4.93\mu m$ (7.2% to 10% of corresponding travels). A similar plot (see Figure 8(b)) obtained for the closed loop configuration shows that the feedback control laws virtually eliminate all hysteretic effects and the output and reference signals match well. In this case, the travel length is $45\mu m$ and the maximum output hysteresis was significantly reduced to 62.3 nm (0.14%) and the corresponding maximum input hysteresis was reduced to 2 mV (0.07%).
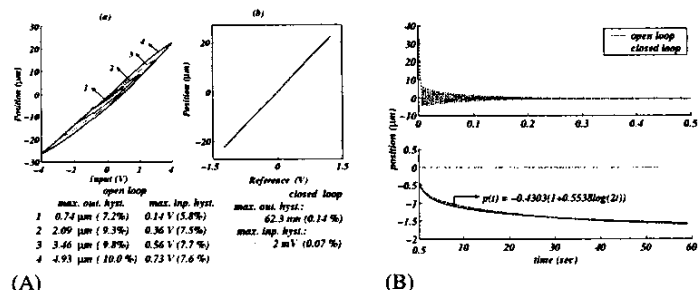

(A)   (B)

Fig. 8. (A) Hysteresis in (a) the open loop configuration, (b) its elimination in the closed loop configuration. (B) (a) responses to the step input of open loop and closed loop systems (b) The elimination of creep in the closed loop system and its approximation by a creep law.

The creep effect is approximately described by the equation,

$$y(t) \approx y_0(1 + \gamma \log(t/t_0)),$$

where t_0 is the time at which the creep effect is discernible, y_0 is the value of the signal at t_0 and γ is a constant, called the creep factor, that characterizes this nonlinear effect. We see that the output in the open loop case responds to the reference signal (see Figure 8) but instead of reaching a steady state value it continues to decrease at a very slow rate. The response $y(t)$ was found to approximately satisfy the creep law with a creep factor of 0.55. The same experiment conducted in the closed loop shows that the feedback laws virtually eliminate this effect and the system tracks the reference signal exactly.

Repeatability

A significant adverse effect of the nonlinearities in the open loop is that of non repeatability. This was seen clearly in the calibration experiment described in the previous section. In the open loop case, the grooves that were observed when travelling in one direction were not concomitant with those in the other direction. Also, the images were distorted in the open loop scans. These effects were removed with feedback control (the results using the $\mathcal{H}_\infty$ controller is shown here. The scanning speeds were beyond the bandwidth achieved by the PI law). The mismatch in the open loop is more clearly seen in the left plot in Figure 9(Left), where the image obtained in one direction is kept behind the one got in the other direction for the sake of comparison. In (c), the near perfect match with the closed loop system is demonstrated.

B. Two dimensional nanopositioning device

This device has the same working principle as the device described in the previous section except that it provides motion in two directions. The flexure stage consists of two stages, 'X' seated on 'Y' (see Figure 9(Right)), with the sample holder on the 'X' stage.

Each stage, by virtue of the serpentine spring design deforms under the application of force providing motion. These forces are generated by stack-piezos. As shown in Figure 9(Right), there are three piezo-actuators in series for each axis. The motion of each stage is measured by the respective LVDT (Linear Variable Differential Transformer) and the associated demodulation circuit. In this device, the control laws are implemented on a *Analog Devices ADSP-21160* digital signal processor.
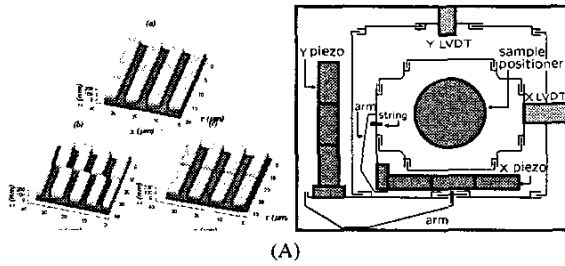
Fig. 9. (A) (a) The reference (calibration sample) geometry. (b) The mismatch in the position of grooves between the forward and the backward traverses in the open loop. (c) a good match in the closed loop configuration. (B) A schematic of the nanopositioning device.

1) Identification:

The device is viewed as a two-input two-output system where the low voltage signals to the 'X' and 'Y' amplifiers (u_x and u_y) are the inputs and the motion of 'X' and 'Y' stages measured by the respective LVDT sensors, (x and y) are the outputs. This results in four input-output transfer functions, $G_{ij}, i, j \in \{x, y\}$. Here G_{ij} represents the transfer function from the input u_j to the output i. These maps were identified using frequency response about the null position. The responses were obtained using a *HP3536A* signal analyzer with 10 mV amplitude forcing and averaged over 200 measurements for a bandwidth of 1.25kHz. $G_{xx}(s)$, a 7th order transfer function with the first resonance frequency at approximately 390 Hz, was fit to the frequency response. $G_{yy}(s)$ is 5th order with the first resonance frequency at 235 Hz. The coupling transfer functions G_{xy} and G_{yx} are negligible compared to the diagonal transfer functions and therefore were neglected in order to simplify the design process. The mode of operation of this device is such that higher bandwidth requirements are made on the smaller stage 'X' where as 'Y' stage is made to move relatively slow. Hence, there is a greater emphasis on the control designs for the 'X' stage which is presented in this paper. Designs were also done for G_{yy} and the resulting diagonal controllers were implemented, the details of which are not presented in this paper. The transfer function G_{xx} is given by

$$\frac{4.29 \times 10^{10}(s^2 + 631.2s + 9.4 \times 10^6)(s^2 + 638.8s + 4.5 \times 10^7)}{(s^2 + 178.2s + 6 \times 10^6)(s^2 + 412.3s + 1.6 \times 10^7)(s^2 + 209.7s + 5.6 \times 10^7)(s + 5818)},$$

and its fit to the experimental data is shown in Figure 10(A). In order to further validate the models, step responses obtained experimentally are compared with the model responses. In Figure 10 (B), a comparison of the step responses shows agreement between the two responses for both G_{xx}. The slight variation in gain could be attributed to hysteresis since the models are obtained using low amplitude (10 mV) signals whereas the step response in this experiment has a magnitude of around 200 mV.

To study the variation of these models to the operating points, frequency responses are obtained at different operating points. A considerable variation was observed in these responses. Figure 10(C) shows the responses obtained at different operating points spread over a range of approximately 80 μm, separated by approximately 20 μm. Further it was observed that the frequency response at the same operating point varies when obtained at different times. These uncertainties in the model make robustness of the closed loop system a key requirement. The design of the feedback laws to achieve these requirements is presented in the next section.

2) Control Design: Proportional double integral (PII) control design

These designs are popular as they are simple to implement. Moreover an attractive feature of these controllers is that they can track ramp signals (common in imaging applications) with zero steady state errors. Here a PII design is presented which has been obtained after considerable search and tuning over the parameter space. It is given by $K_{pii}(s) = \frac{0.001s^2 + 450s + 10^5}{s^2}$. This controller was implemented and the experimental bode plot of S is shown in Figure 10(E). Besides having a low closed loop bandwidth of 37 Hz, this design has poor robustness properties. The tracking of signals with frequencies as low as 5 Hz is unsatisfactory. This shows that the usable region of the trajectory is only 30% of the total period (see

Figure 10(D). The $\|S\|_\infty$ for K_{pii} is 13.8 dB which results in lower bounds on GM and PM of 1.25 and 11.73 degrees respectively. Due to the low phase margin, attempts to introduce a low pass filter within the loop to improve the resolution results in instability.

$\mathcal{H}_\infty$ control design

A nominal $\mathcal{H}_\infty$ design was done for this system on the same lines as done for the one dimensional device. The controller was found to be non-robust and was found to have poor noise characteristics after implementation. The reason for this behavior is that the nominal $\mathcal{H}_\infty$ design does not account for pole uncertainties which are crucial for G_{xx} which has lightly damped poles. The nominal $\mathcal{H}_\infty$ controller has zeros at 389 Hz which is a dominant pole of G_{xx} which is also lightly damped. See Ref. [16] for a detailed description of these pole-zero cancellations in nominal $\mathcal{H}_\infty$ designs. Nominal $\mathcal{H}_\infty$ design without consideration for robustness is found to be inappropriate for the nanopositioner. Robust $\mathcal{H}_\infty$ designs which account for pole uncertainties is one way of tackling this problem at the expense of bandwidth.

Robust $\mathcal{H}_\infty$ design

In this design, The pole uncertainty in G_{xx} is characterized using multiplicative uncertainty. It can be shown that if a controller has to satisfy $\|w_p S\|_\infty \leq 1$ for plants belonging to a class $\mathcal{G}_{xx} = \{G_{xx}(1 + w_i \Delta) : \|\Delta\|_\infty \leq 1\}$, then it is sufficient that,

$$\left\| \begin{matrix} w_p S \\ w_i T \end{matrix} \right\|_\infty \leq 1/\sqrt{2} \text{ is satisfied (see Ref. [15]). So in the original}$$

nominal $\mathcal{H}_\infty$ problem, the selection of $w_T = w_i$ fetches robust performance instead of just nominal performance. For G_{xx}, w_i was selected to be,

$$w_i(s) = \frac{0.84s^2 + 2214s + 5.3 \times 10^6}{s^2 + 575.5s + 6.12 \times 10^6}.$$

In the original $\mathcal{H}_\infty$ problem, w_T was chosen to be w_i to incorporate the added robust performance requirement. The resulting controller was 13th order given by,

$$\frac{10617.6(s + 1.5 \times 10^4)(s + 5818)(s + 1717)(s + 214.8)(s^2 + 1082s + 5.17 \times 10^6)}{s + 1.85 \times 10^4)(s + 4.7)^2(s^2 + 2908s + 3.88 \times 10^6)(s^2 + 4167s + 7.2 \times 10^6)}$$
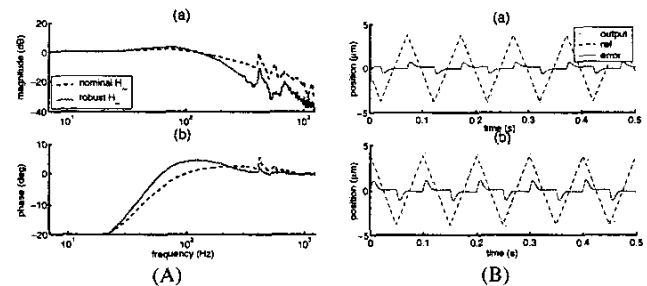

Fig. 11. (A) The sensitivity and complementary sensitivity functions are compared for nominal and robust $\mathcal{H}_\infty$ designs. (B) a) Tracking of a 10Hz triangular signal using an $\mathcal{H}_\infty$ controller. b) Tracking of the same signal using a robust $\mathcal{H}_\infty$ controller.

The experimental plots are compared in Figure 11. It can be seen that the experimental closed loop transfer function plots have some features absent in the analytical plots. This is due to uncertainty in the plant model, particularly pole uncertainty. Figure 11 shows the experimental result of how the robust design introduces a dip in this frequency region thus reducing the magnitude of these unwanted peaks shows a 5 times reduction in the unwanted peak at near the dominant pole location due to the robust design). The right plot in the figure shows the tracking of 10 Hz triangular waves by nominal $\mathcal{H}_\infty$ and robust $\mathcal{H}_\infty$ controllers.
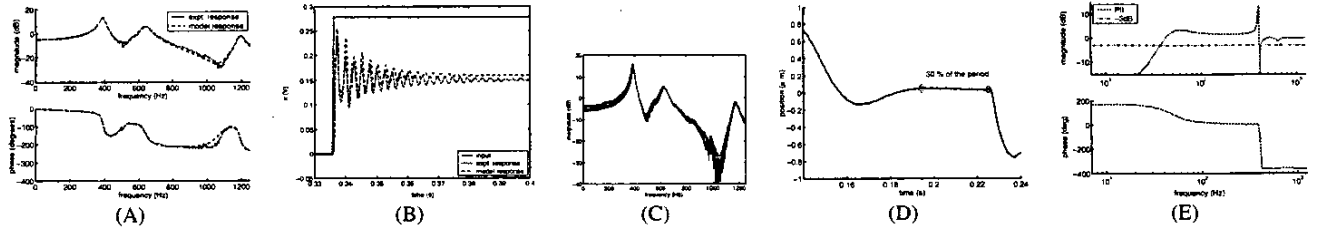
Glover-McFarlane control design

Fig. 10. (A) Experimental frequency response is compared with the response of the model $G_{xx}(s)$. (B) The experimental step response is compared with the response of G_{xx}. (C) Experimentally obtained frequency responses at different operating regions for the X stage. (D) At 5 Hz, oscillatory behavior is observed which reduces the region of the trajectory which can be used for scanning purposes. (E) The experimental bode plot of the sensitivity function is shown for a PII controller.
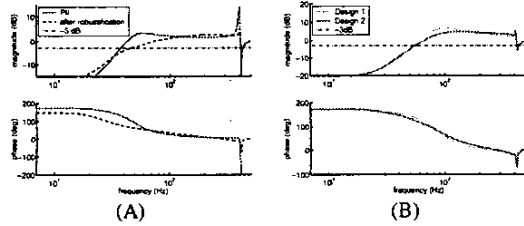

Fig. 12. (A) Experimentally obtained $S(j\omega)$ of K_{pii1} before and after robustification. (B) Experimentally obtained sensitivity functions of the Glover McFarlane designs.

This design (see Ref. [17] and Ref. [18]) addresses *simultaneously* both the performance and robustness requirements. A remarkable feature of this design is that it achieves robustness with marginal reduction in performance. In fact, it is able to quantify the reduction by determining explicit bounds on how much it changes the loop gains at low and high frequencies. This design process consists of two steps: one in which a controller K_s is designed to meet performance objectives and the other in which a controller K_r is designed to attain robustness.

The uncertainty (in the second step) is modelled as a combination of uncertainty in the numerator polynomial and the denominator polynomial of the nominal loop transfer function (GK_s). This characterization is very relevant to nanopositioning devices as it accounts for the plants with poles which are close to imaginary axis (as in the model of this device) and thus avoids control laws that "cancel" this poles. The robustness of the design is measured in terms of ϵ which is called the stability margin (see [15] pages 377-380). It is a one shot design (unlike the iterative process of $\mathcal{H}_\infty$ design) and directly characterizes the tolerable uncertainty. Another important feature of the Glover McFarlane design is that the loop transfer function before and after robustification is not significantly different (see [18] for details).

Robustification of K_{pii}

The design process was applied to G_{xx} with K_s set to K_{pii} from previous subsection. A 9th order robustifying controller K_r was obtained which is given by,

$$K_r(s) = \frac{5227.6(s + 5818)(s + 31.45)(s^2 + 160.3s + 5.98 \times 10^6)}{(s + 2797)(s + 5684)(s + 294.8)(s^2 + 386.2s + 6.6 \times 10^6)}$$
$$\times \frac{(s^2 + 209.6s + 5.6 \times 10^7)}{(s^2 + 397.3s + 1.66 \times 10^7)(s^2 + 203.3s + 5.62 \times 10^7)}.$$

Figure 12(A) compares the experimentally obtained $S(j\omega)$ for K_{pii} before and after robustification. There is substantial reduction in the peak of $|S(j\omega)|$ due to the robustifying controller. The resulting lower bounds for GM and PM for the Glover McFarlane design is 2.3 and 33 degrees respectively which are significantly higher than 1.25 and 11.73 degrees for K_{pii}. Note that the bandwidth is comparable for both in spite of the significant difference in robustness.

More aggressive PII controllers can be implemented as the first step of the design does not impose stability requirements.

In Figure 12(B), the sensitivity function (experimental) of two such designs are shown. Designs 1 and 2 correspond to PII controllers $\frac{0.001s^2 + 600s + 6 \times 10^5}{s^2}$ and $\frac{0.01s^2 + 500s + 5 \times 10^5}{s^2}$ respectively. The PII controller in design 1 if used without robustification results in instability of the closed loop. However with robustification, these designs are stable and they guarantee good robustness margins with the added benefit of increased performance. The plots show significant increase in bandwidth (> 55 Hz) without much loss in robustness (GM greater than 1.9 and PM greater than 29 degrees).

Triangular signals are tracked using the implemented Glover McFarlane designs. Figure 13(A) illustrates the tracking of 5 Hz and 10 Hz signals using the Glover McFarlane design 2. Except for the turn around points the tracking error is small. For the 5 Hz triangular signals, approximately 70% of the period is usable in this case compared to 30% for K_{pii} in spite of the larger amplitude of the reference waveform. Also these controllers are remarkably robust allowing the use of filters inside the loop to improve resolution. Since the performance and robustness requirements are decoupled, Glover McFarlane controllers can be used to robustify commonly used controllers like PII which have features like zero steady state error for ramp tracking. This is a significant advantage particularly when the nanopositioner is used for scanning applications.

3) Characterization of the device: In this section the device is characterized in terms of static sensitivity, range, resolution, in the open and closed loop configurations. The Glover McFarlane design 2 described in section II-B.2 is presented as an example.

Static sensitivity and travel range

The device was calibrated using a micro-cantilever and a 10 micron grating with 200 nm deep grooves. The range of the LVDT output was 16.27 V and the corresponding cantilever deflection showed the presence of 11 grooves which correspond to 110 μm. Hence the sensitivity of the X LVDT was found to be 6.76 $\mu m/V$.

Resolution

Since this device has no backlash (as there are no sliding parts) or any other such design restrictions, the resolution of the device is primarily determined by noise. However, this makes the comparison of resolution between the open and the closed loop configurations difficult. We emphasize here that though theoretically the open-loop resolutions are better (which may possibly be realized with very rigorous experiments and post data processing), it is much easier to predict and *realize* accurate positioning in the closed loop designs.

The resolution can be characterized by associating appropriate metrics to the error signals $e_x = Tn$ if enough statistics describing n is available. However, our measurements are limited by the resolution of the LVDT sensors, i.e., the device is capable of motions that are smaller than which LVDT can detect. However, to get a quantitative feel of how small these error signals can be, the following experiment was done. The LVDT signals for both the open-loop and the closed-loop (Glover McFarlane) designs were measured when the system is at the nominal operating point. The measurement is taken over a small time window since in open loop the mean varies with drift, creep etc. Figure 13(B) shows that the variance of the sensor output while in open loop
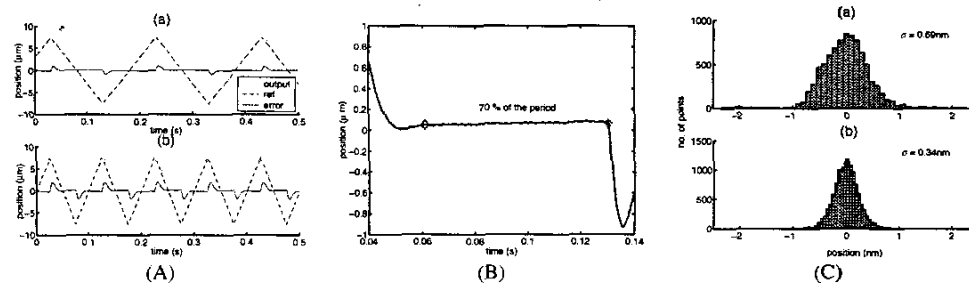
Fig. 13. (A) Tracking of 5 Hz and 10 Hz triangular signals using a Glover McFarlane controller. For the 5 Hz triangular signals, almost 70% of the period is usable in this case. (B) a) LVDT measurement without the controller. b) LVDT measurement while a controller is stabilizing at 0V.

is higher than that in closed loop. This illustrates the improvement in 'resolution' due to feedback. It should be remembered that the closed loop resolution depends on the bandwidth and the shape of the corresponding complementary sensitivity functions. Better resolutions can be achieved by reducing the bandwidths.

III. CONCLUSIONS

We have presented the demands and challenges on nanopositioning devices. It has been shown that they fall naturally into the modern control theory paradigm. This theory provides an appropriate approach to quantify, incorporate and achieve both the performance and robustness objectives. Using this approach, we have obtained improvements of over sixty times in bandwidth and repeatable subnanometer resolution for these devices. The implementation of the Glover Mcfarlane design achieved substantial improvements in the robustness properties of previously designed PII controllers. One of the future goals is to design smaller positioning systems (to achieve higher bandwidths) and tackle the large "coupling" effects by designing appropriate MIMO controllers. Another aim is to use preview based methods to obtain better tracking of a priori known reference signals.

IV. REFERENCES

[1] D.L. White and O.R. Wood. Novel alignment system for imprint lithography. In Jurnal of Vacuum Science & Technology B (microelectronics and Nanometer structures), Rancho Mirage, volume 18(6), pages 3552–3556, May-June 2000.

[2] M. Jianxu and M.H. Ang Jr. High-bandwidth macro/microroactuation for hard disk drive. In Proceedings of the SPIE- the International Society for Optical Engineering, Boston, volume 4194, pages 94–102, November 2000.

[3] Z. Rihong, Daocai X., Y. Zhixing, and C. Jinbang. Research on systems for measurements of CCD parameters. In Proceedings of the SPIE- the International Society for Optical Engineering, volume 3553, pages 297–301, September 1998.

[4] D. Krogmann, H.D. Tholl, P. Schreiber, A. Krehl, R. Goring, B. Gotz, and Th. Martin. Image multiplexing system on the base of piezoelectrically driven silicon microlens arrays. In 3rd International Conference on Micro Opto Electro Mechanical Systems, MOEMS 99, Mainz, Germany., pages 178–185, August-September 1999.

[5] D.R. Meldrum, W.H. Pence, S.E. Moody, D.L. Cunningham, M. Holl, P.J. Wiktor, M. Saini, M.P. Moore, L-S Jang, M. Kidd, C. Fisher, and A. Cookson. Automated, integrated modules for fluid handling, thermal cycling and purification of dna samples for high throughput sequencing and analysis. In Proceedings of 2001 IEEE/ASME International conference on Advanced Intelligent Mekatronics, volume 2, pages 1211–1219, July 2001.

[6] G.M. Whitesides and H.C. Love. The art of building small. Scientific American, 285(3):39–47, September 2001.

[7] R. Koops and G.A. Sawatzky. New scanning device for scanning tunneling microscope applications. Review of Scientific Instruments, 63(8):4008–9, August 1992.

[8] H. Kaizuka. Application of capacitor insertion method to scanning tunneling microscopes. Rev. of Sci. Instrum., 60(10):3119–3122, 1989.

[9] R.C. Barrett and C.F. Quate. Optical scan-correction system applied to atomic force microscopy. Rev. of Sci. Instrum., 62:1393–1399, 1991.

[10] D. Croft, G. Shedd, and S. Devasia. Creep, Hysteresis and Vibration compensation for Piezoactuators: Atomic Force Microscopy Application. In Proceedings of the American Control Conference, Chicago, Illinois, pages 2123–2128, June 2000.

[11] A. Daniele, S. Salapaka, M.V. Salapaka, and M. Dahleh. Piezoelectric Scanners for Atomic Force Microscopes:Design of Lateral Sensors, Identification and Control. In Proceedings of the American Control Conference, San Diego, California, pages 253–257, June 1999.

[12] G. Schitter, P. Menold, H. F. Knapp, F. Allgower, and A. Stemmer. High performance feedback for fast scanning atomic force microscopes. Review of Scientific Instruments, 72(8):3320–3327, August 2001.

[13] S. Salapaka, A. Sebastian, J. P. Cleveland, and M. V. Salapaka. High bandwidth nano-positioner: A robust control approach. Review of Scientific Instruments, 73(9):3232–3241, September 2002.

[14] A. Sebastian and S. Salapaka. $\langle_\infty$ loop shaping design for nano-positioning. In Proceedings of the American Control Conference, Denver, Colorado, page to appear, June 2003.

[15] S. Skogestad and I. Postlethwaite. Multivariable Feedback Control, Analysis and Design. John Wiley and Sons, 1997.

[16] J. Sefton and K. Glover. Pole/zero cancellations in the general $\mathcal{H}_\infty$ problem with reference to a two block design. Systems and Control Letters, 14(4), 1990.

[17] K. Glover and D. McFarlane. Robust stabilization of normalized coprime factor plant descriptions with $\mathcal{H}_\infty$-bounded uncertainty. IEEE transactions on automatic control, 34(8):821–830, August 1989.

[18] D. McFarlane and K. Glover. A loop shaping design procedure using $\mathcal{H}_\infty$ synthesis. IEEE transactions on automatic control, 37(6):759–769, June 1992.